RSC Advances

PAPER

View Article Online
View Journal | View Issue

Cite this: *RSC Adv.*, 2018, **8**, 37880

Introducing catalytic gasification into chemical activation for the conversion of natural coal into hierarchically porous carbons with broadened pore size for enhanced supercapacitive utilization†

Tong Pei, Fei Sun, * Jihui Gao, Lijie Wang, Xinxin Pi, Zhipeng Qie and Guangbo Zhao

Focusing on engineering the pore structure of porous carbons for enhanced supercapacitive performances, a new type of coal derived hierarchically porous carbon which is synthesized by introducing a catalytic gasification mechanism into an often-utilized chemical activation process is demonstrated. Such a strategy skillfully employs the catalytic effects of the minerals in natural coal on the etching reaction between CO_2 molecules and carbon framework, which easily widen the pore size of well-developed micropores, thereby yielding a hierarchical pore configuration with simultaneously high surface area, large pore volume as well as broadened pore size distribution. The enhanced pore development mechanism is elucidated by a series of control experiments and thermogravimetric analysis. Evaluated as supercapacitor electrode materials, the resulting HPC exhibits state-of-the-art supercapacitive performances in both aqueous and non-aqueous electrolytes, particularly the superior rate capabilities, which highlights the favorable role of broadened pore configuration in facilitating electrolyte ion transfer and storage. Combining with the naturally abundant carbon resource and easily-implemented preparation craft, the as-obtained coal transferred hierarchically porous carbons hold great potentials for industrial production and supercapacitor applications.

Received 2nd September 2018
Accepted 2nd November 2018

DOI: 10.1039/c8ra07308b

rsc.li/rsc-advances

1. Introduction

The developments of advanced energy storage systems are urgently needed to meet the rapidly growing demands of electronic devices, hybrid electric vehicles and large-scale energy storage,[1–3] which undoubtedly rely on the rational design of advanced energy materials with special properties. Porous carbon materials, because of their easily-tunable porosity/framework, excellent physicochemical compatibility and abundant synthetic resources, have been widely explored and applied in the fields of electrochemical energy storage (EES) such as supercapacitors (SCs),[4,5] lithium ion batteries (LIBs)[6] and sodium ion batteries (SIBs).[7,8] Among the numerous structural characteristics for porous carbons, pore structure and surface chemistry have been regarded as the most important factors influencing the energy storage process.[9] Taking the supercapacitor as an example, it stores charges by the electrostatic adsorption or accumulation of electrolyte ions onto the surface of porous carbon electrodes by which high porosity and large specific surface area (SSA) are beneficial to the improvement of capacitance. Besides, doping heteroatoms into porous carbon framework has been demonstrated effective to change the electronic properties and polarity of carbon structure and hence improve the rate and capacity performances of constructed electrodes.

To boost the capacitive properties of porous carbon materials, substantial progresses have been made on engineering the porous structure, for instance, microporous carbon,[10,11] mesoporous carbon[12] and especially, hierarchical porous carbon.[13–15] Moreover, owing to the pseudocapacitive effect of heteroatom doped on carbon materials, doping carbon materials also have explored, for instance, Fu *et al.* have worked on nitrogen doped porous carbon materials,[16–18] in addition, oxygen,[19] phosphorus,[20] boron[21] and sulfur[22,23] also arouse the attention of the researchers. Besides, considering the cost and resource abundance, in recent years, porous carbons derived from natural biomass and coals have been extensively excavated and show incremental improvements in EES utilizations.[24–26] Among the reported biomass/coal converted porous carbons, a chemical activation procedure which employ KOH,[27–29] K_2CO_3,[30] $ZnCl_2$ [31,32] and H_3PO_4 [33,34] as activation agents is frequently used to create abundant porosity. Despite these achievements in developing high surface area porous carbons, the often-utilized chemical activation method commonly leads to the formation of dominantly microporous structure which, compared with

School of Energy Science and Engineering, Harbin Institute of Technology, Harbin 150001, Heilongjiang, China. E-mail: sunf@hit.edu.cn

† Electronic supplementary information (ESI) available. See DOI: 10.1039/c8ra07308b

mesoporous or hierarchically porous configuration, may pose unfavorable impacts on electrolyte transfer and buffering, consequently leading to inferior rate capability of constructed electrodes. Thus, it is still desirable to develop new strategies for preparing low-cost porous carbons with simultaneously high surface area and favorable pore configuration to achieve the synergistic optimization of rate and capacity capability of constructed supercapacitors.[9]

In this work, we demonstrate a facile synthesis of a new type of hierarchically porous carbons using Chinese large-reserve Zhundong natural coal as starting materials (exploitable reserve of 164 Gt[35] in Xinjiang district, China). The preparation is achieved by ably introducing catalytic gasification mechanism into traditional activation process with CO_2 as the activation atmosphere during which chemical activation leads to the formation of abundant micropores while the natural minerals in raw coal effectively catalyze the gasification reaction between CO_2 and coal framework, easily widening the pore size. The mineral-assisted catalytic activation and chemical activation are integrated in one heat-treatment procedure and result in a synergism that enable the resulting porous carbon (denoted as HPC) with a hierarchical pore configuration possessing simultaneous high surface area and broadened pore size distribution. Compared with the microporous carbon (denoted as MPC) prepared by solely chemical activation, the as-obtained HPC show both higher pore parameters and better pore configuration, endowing the constructed supercapacitor electrode with high capacitances, excellent rate capabilities and long cycling stability in both aqueous and organic systems. At high current rates of higher than 30 A g^{-1}, the HPC electrode exhibits near constant capacitance in an aqueous electrolyte system; even at an ultra-high current density of 100 A g^{-1}, it can still maintain around 200 F g^{-1}, indicating a rapid charge–discharge performance. Moreover, such well-developed pore structure of HPC also enables superior cathode performances for lithium ion capacitors, including large capacity (127 mA h g^{-1} at 0.3 A g^{-1}), high rate capability (still 78 mA h g^{-1} at 10 A g^{-1}) as well as excellent cycling stability (88% capacity retention after 5000 cycles at a current rate of 2 A g^{-1}).

2. Experimental

2.1 Sample preparation

The hierarchically porous carbon (HPC) was prepared by introducing mineral-assisted catalytic gasification mechanism into a H_3PO_4 activation process with CO_2 as the activation atmosphere. In a typical procedure, dried Zhundong coal with particle size less than 0.25 mm was mixed with H_3PO_4 at a mass ratio of 1 : 2 under stirring at 80 °C. Then the mixture was dried in a hot air oven at 110 °C. Subsequently, 6 g coal and H_3PO_4 mixture was placed into a crucible in a horizontal furnace, which was heated to 500 °C for 2 h and subsequently heated to 950 °C for 1 h. The reaction atmosphere was a mixture of CO_2 (40 mL min^{-1}) and N_2 (160 mL min^{-1}). After cooling, the samples were washed with 2 M hydrochloric acid, 10 wt% hydrofluoric acid and deionized water to remove the inorganic impurities. Finally, the samples were dried in hot air oven at 80 °C overnight to obtain HPC.

Control sample preparation. In order to investigate the catalysis gasification effect on the porosity development of the hierarchically carbons, a solely H_3PO_4 activation procedure was also carried out, which was similar to the above process at 500 °C for 2 h or further heated to 950 °C for 1 h under inert N_2 atmosphere. The prepared porous carbons were denoted as MPC-500 and MPC-950, respectively. In order to demonstrate the role of inherent minerals, demineralized coal was firstly prepared and used as mineral-free starting material. The demineralization process was carried out by using 5 M hydrochloric acid and 10 wt% hydrofluoric acid to completely remove minerals and impurities. After demineralization, the mineral-free coal was treated in exactly the same operating procedure as HPC. The resulting porous carbon was denoted as MF-PC where MF represents Mineral Free.

2.2 Characterizations

The morphology of the as-prepared samples was characterized by scanning electron microscopy (SEM, Helios Nanolab600i) and transmission electron microscopy (TEM, JEM-2100). The structure and composition of the samples were analyzed by X-ray diffraction (XRD), which were obtained on a Rigaku D/Max 2400 diffractometer using Cu Kα radiation at 40 kV and 40 mA (λ = 1.5406 Å) and Raman spectroscopy (NT-MDT NANO-FINDER). Moreover, X-ray photoelectron spectroscopy (XPS) analysis was conducted on a PHI 5700 ESCA System with Al Kα X-ray (14 kV, 6 mA). The adsorption/desorption isotherms of the samples were measured at −196 °C using ASAP 2420 (V2.05) apparatus. The porosity properties of the samples were obtained using the Brunauer–Emmett–Teller (BET) equation. The pore size distributions of the samples were calculated by Density Functional Theory (DFT) based on the adsorption branch.

2.3 Electrochemical measurement

The electrochemical performances of the as-prepared materials were investigated in both aqueous (6 M KOH) and organic (1 M $LiPF_6$ in ethylene carbonate and diethyl carbonate (EC/DEC, v/v = 1 : 1)) electrolytes at room temperature. To fabricate the electrodes, the obtained porous carbons (80 wt%) were mixed with carbon black (10 wt%) and polytetrafluoroethylene (PTFE) (10 wt%) homogeneously. Then the mixture was rolled into a thin film and dried at 100 °C for 12 h. For the fabrication of HPC electrode in aqueous test, the prepared materials were loaded onto the nickel foam with a mass loading of 3 mg and the working electrode obtained. Pt foil and calomel electrode (SCE) were used as the counter electrode and reference electrode, respectively. For the fabrication of HPC electrode in organic test, the prepared materials were casted on the carbon-coated aluminum foil with ~2 mg cm^{-2} mass loading. A 2032-type coin cell was assembled in the glove box using lithium foil as counter and reference electrode and Glass fiber (GF/D) as separator. Cyclic voltammetry and chronopotentiometry were carried out at CHI660E. The electrochemical impedance

spectroscopy tests were conducted by a Solartron 1287/1260 electrochemical workstation over a frequency range from 100 kHz to 10 MHz at an amplitude of 10 mV. The specific gravimetric capacitances (C_s, F g^{-1}) were calculated by the equation: $C_s = \frac{I\Delta t}{m\Delta V}$, where I is the constant discharge current, Δt is the time for the full discharge, m is the mass of active materials in the working electrode, and ΔV represents the voltage window (exclude the internal resistance drop).[22]

3. Results and discussion

3.1 Preparation of hierarchical porous carbon (HPC)

The preparation of the coal converted HPC is achieved by introducing catalytic gasification mechanism into H_3PO_4 activation process with CO_2 as the activation atmosphere during which the embedded mineral species play a significant role in catalyzing the etching reaction between CO_2 and coal framework, as illustrated in Fig. 1. As comparison, the preparation of microporous carbon (MPC) by solely H_3PO_4 activation with inert N_2 as reaction atmosphere is also illustrated for demonstrating the catalytic gasification effects on porosity developments. Firstly, the raw coal particles were mixed with H_3PO_4 to obtain a homogeneous mixture. For the solely H_3PO_4 chemical activation process, the mixture experiences a N_2 protected heat treatment procedure during which the reaction between H_3PO_4 and coal occur under temperature higher than 500 °C. First, in the impregnation process, the ionization of phosphoric acid causes the cross-linked structure to swell up, then H_3PO_4 molecules intercalate into the internal structure, forming a homogeneous precursor. During the activation process, phosphoric acid has a strong dehydration effect, promoting the elimination of hydroxyl groups. Phosphoric acid further incorporates into the coal framework, forming polymerization products of phosphate and polyphosphate compounds.[36] Finally, phosphoric acid also plays a skeletal role in the activation process and accompanies by the formation of micropores.[37–40] This process is usually carried out at a relatively low temperature at around 500 °C.[41,42] Once the reaction atmosphere is replaced by carbon dioxide, a catalytic gasification reaction between CO_2 and coal structure is introduced, which poses significant impacts on the porosity development of resulting carbons. In detail, CO_2 can react with coal framework to create pores under temperature higher than 800 °C (called gasification reaction, the Boudouard reaction starts: $CO_2 + C = 2CO$). Most researchers believe that diffusion control regime is approximately above 900 °C.[43–46] In order to ensure the gas utilization efficiency during the material preparation process, we choose 950 °C as the catalytic activation temperature since it is in diffusion control regime. Moreover, the employed Zhundong raw coal is rich of various mineral species (especially alkali and alkaline earth metals, AAEM, as shown in Table S1 and S2†). Catalytic gasification is a redox process. During the heating process, mineral species may change to different solid phase (or liquid phase) in the two interfaces, getting equilibrium with carbon structure and gas phase; then the minerals promote the electron transfer process, during which CO_2 molecules adsorbed on the free carbon active site and decomposed into CO; finally the carbon bulk diffusion occurs and the coal framework was etched.[47] The general mechanism is expressed as follows:[48]

$$C_f + CO_2 \rightarrow C_f(CO_2) \quad (3\text{-}1)$$

$$C_f(CO_2) \rightarrow C_f(O) + CO \quad (3\text{-}2)$$

$$C_f(O) + C \rightarrow CO + C_f \quad (3\text{-}3)$$

where C_f represents the free carbon active site, $C_f(CO_2)$ represents the CO_2 absorbed on the free carbon active site and $C_f(O)$ denotes the reactive carbon–oxygen surface complex. During this process, the catalyst particles move on the base surface or erode from the edge to the inside or combine the two ways of etching together, effectively catalyzing the gasification reaction between CO_2 molecule and coal structure which broadened micropores to meso-/macropores. This has been demonstrated in our previous study.[49] Thus, the mineral-assisted catalytic

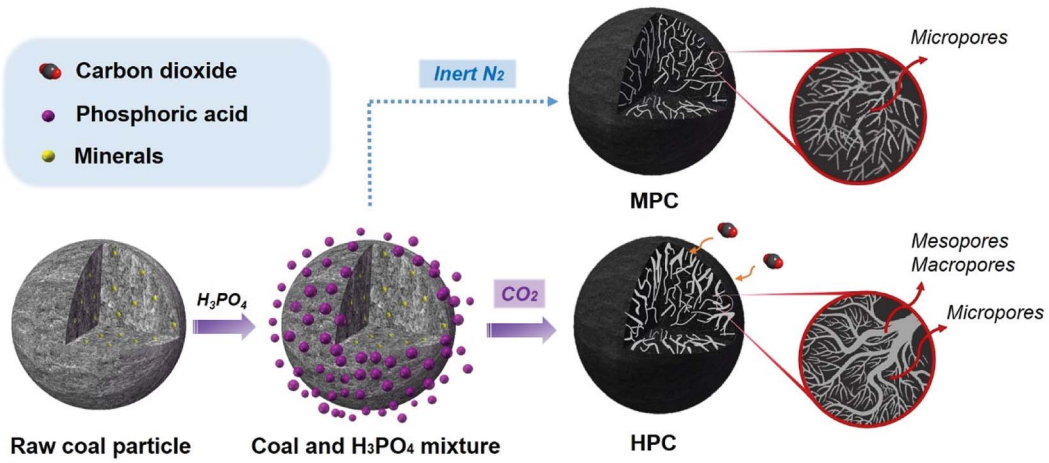

Fig. 1 A schematic illustration of the porosity construction and development mechanism under different processing conditions.

activation and H_3PO_4 chemical activation are integrated in one CO_2-assisted heat-treatment procedure where H_3PO_4 chemical activation leads to the creation of abundant micropores while mineral-assisted catalytic gasification promotes the formation of larger size mesopore and/or macropores. These two effects result in a synergism that enable the resulting porous carbon (denoted as HPC) with a favorable micropore–mesopore/macropore interconnected hierarchical pore configuration.

3.2 Structural characterizations

To explain and demonstrate synthesis mechanism, the structural information of both coal precursor and derived porous carbons under various preparation conditions are systematically investigated. Fig. 2 shows the representative SEM and TEM image of Zhundong raw coal, MPC derived from solely H_3PO_4 chemical activation and HPC obtained from catalytic gasification coupled activation process. Fig. 2a and b shows the micromorphology of Zhundong raw coal which consists of a large amount of aggregated microcrystals (Fig. 2a) with smooth surfaces (Fig. 2b). Fig. 2c shows the TEM image of Zhundong coal, revealing a compacted laminar structure similar to multilayer graphite. Experiencing a low temperature (500 °C) H_3PO_4 chemical activation process, the resulted MPC-500 still exhibits an aggregated plate structure similar to Zhundong raw coal (Fig. 2d) with some debris on the outer-surface. The amplified SEM image of MPC-500 in Fig. 2e shows a rougher surface morphology, as compared with raw coal, largely due to the etching effects of activating agent. The TEM image of MPC-500 shown in Fig. 2f suggests that after the chemical activation, the sheet structure of raw coal is well conserved, however, with fewer layers due to the activation effects. Fig. 2g–i present the SEM and TEM images of HPC, which show great differences between raw coal and MPC-500. More specifically, both Fig. 2g and h exhibit much more cracked and coarse structures compared with Zhundong raw coal MPC-500, indicating the more intense carbon etching reactions. Fig. 2i presents the TEM image of HPC which demonstrates thinner layered structure than coal precursor (Fig. 2c) and chemical activation derived MPC-500 (Fig. 2f) because of the combined effects of chemical activation of catalytic activation. Thus, it could be concluded that activation conditions pose significant impacts on the carbon structure evolution of Zhundong coal, hence inducing different pore development patterns, which will be discussed shortly. Fig. S1 and S2† show the high-resolution TEM, XRD and Raman results of typical samples, all of which demonstrate the

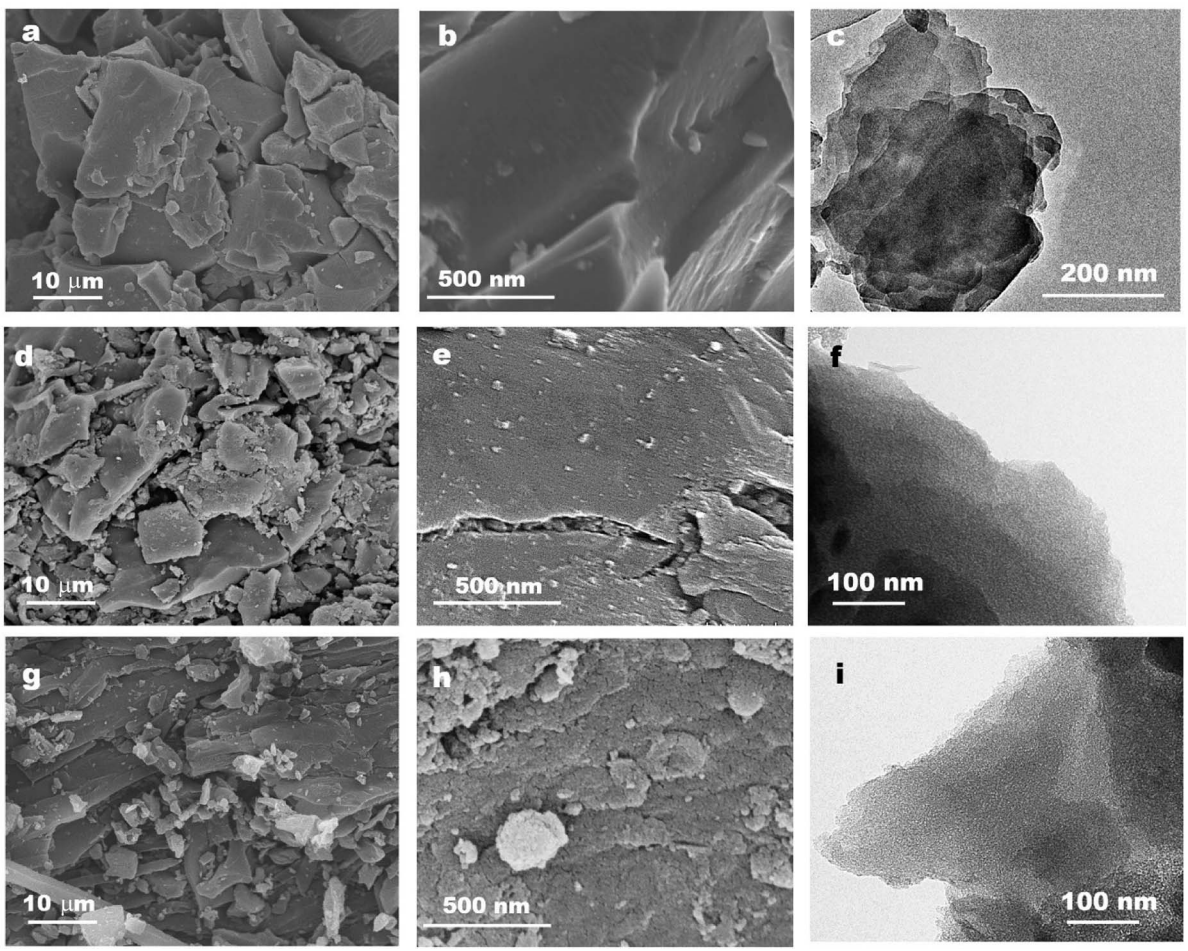

Fig. 2 SEM and TEM of the prepared samples. (a and b) SEM image of Zhundong raw coal; (c) TEM image of Zhundong raw coal; (d and e) SEM image of MPC-500; (f) TEM image of MPC-500; (g and h) SEM image of HPC; (i) TEM image of HPC.

Table 1 Physicochemical parameters and specific capacitances of obtained samples[a]

Samples	S_{BET} ($m^2\ g^{-1}$)	V_t ($cm^3\ g^{-1}$)	XPS (at%) C	O	P	C_s@1 A g^{-1} (F g^{-1})	C_s@100 A g^{-1} (F g^{-1})
MPC-500	975	0.53	92.27	5.74	2.00	145	96.8
MPC-950	1157	0.62	92.78	5.81	1.41	—	—
HPC	2308	1.51	94.94	3.69	1.37	308	202
MF-PC	2105	1.18	94.23	4.32	1.45	—	—

[a] S_{BET}: BET surface area; V_t: total pore volume obtained at P/P_0 of 0.97; C_s: specific capacitance.

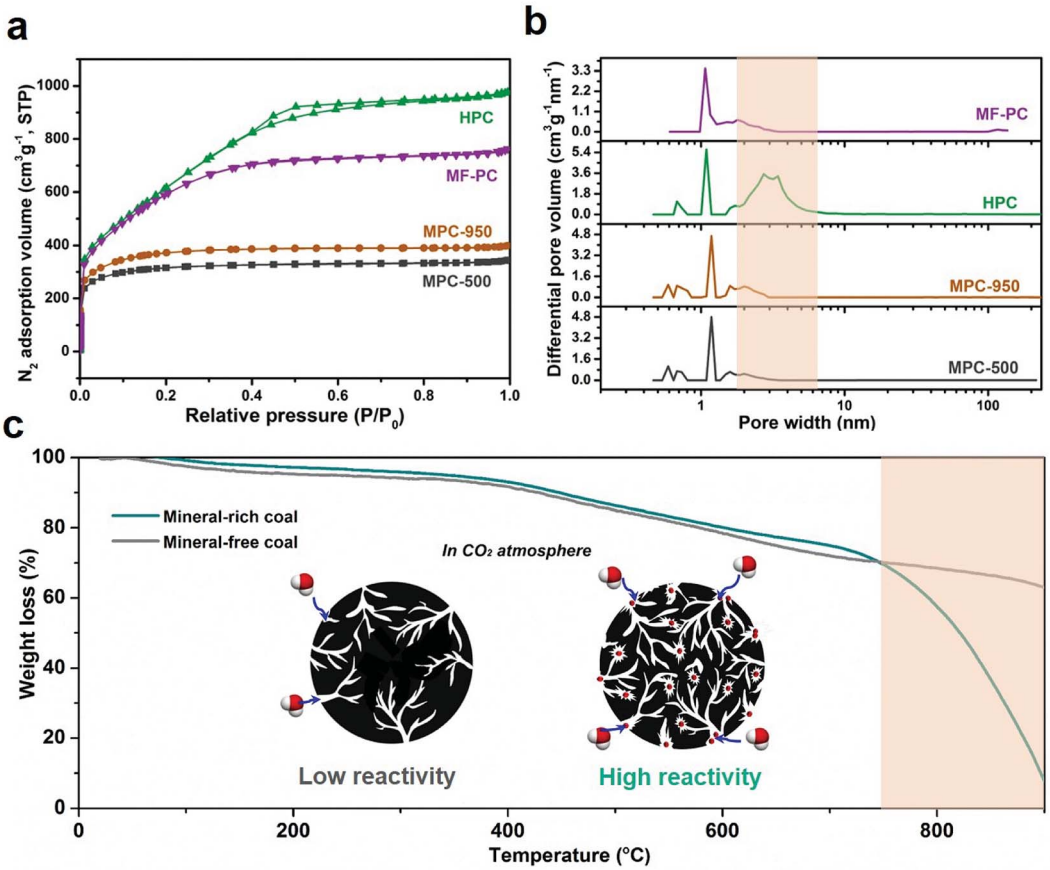

Fig. 3 (a) N_2 adsorption/desorption isotherms of various porous carbon samples; (b) corresponding DFT pore size distributions of various porous carbon samples; (c) thermogravimetry (TG) curves of mineral-rich Zhundong raw coal and mineral-free Zhundong coal under CO_2 atmosphere. Inset illustrates the pore formation activities for mineral-free Zhundong coal and Zhundong raw coal.

mainly amorphous carbon nature of prepared porous carbons (detained discussion seeing ESI†).

The pore structure and corresponding pore size distributions of various coal derived PCs are obtained by nitrogen adsorption/desorption isotherms, as illustrated in Fig. 2a and b. Table 1 shows the pore parameters of prepared carbon materials. As can be observed from Fig. 3a, MPC-500 and MPC-950 obtained by solely H_3PO_4 chemical activation under 500 °C and 950 °C display typical type-I adsorption isotherms with significant nitrogen uptakes at a relative pressure less than 0.1 indicating the dominant microporous structure. Moreover, by comparing the N_2 isotherms of MPC-500 and MPC-950, the increase of chemical activation temperature is not conducive to the development of pores mainly due to the excessive etching of carbon framework. Compared with MPCs from solely chemical activation, the HPC exhibits both increased porosity and broadened pore distribution. The N_2 isotherm of HPC (Fig. 3a) shows combined characteristics of type I and IV isotherm curves, with obvious loop at a relative pressure of 0.4–0.8, indicating the hierarchically porous structure with the co-existence of micropores, mesopores and/or macropores. These results directly demonstrate that the introduction of CO_2 gasification greatly promotes the development of mesopores and/or macropores. To further demonstrate the mineral effects on pore

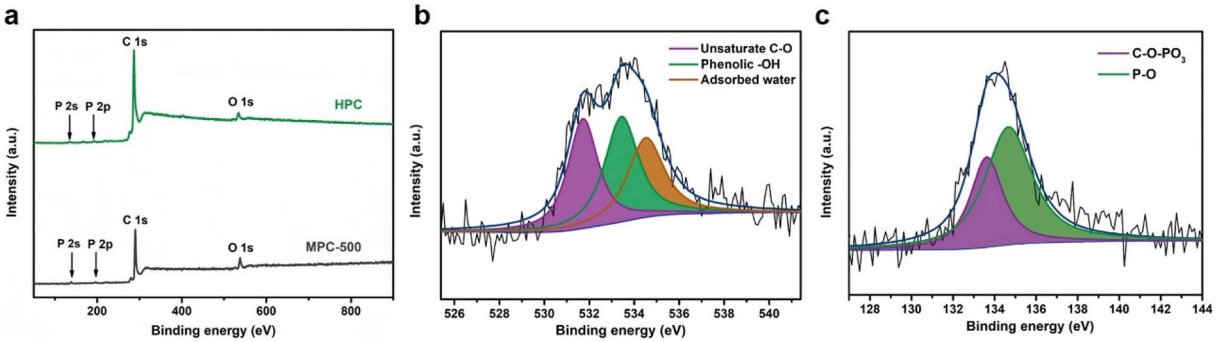

Fig. 4 (a) XPS spectra of MPC-500 and HPC; (b) deconvolution of the O 1s peak of HPC; (c) deconvolution of the P 2p peak of HPC.

development, demineralized Zhundong coal was employed as precursor which experienced the same CO_2-assisted activation process as HPC to obtain the porous carbon (denoted as MF-PC where MF represents mineral-free). The N_2 isotherm of MF-PC is also compared in Fig. 3a. It can be observed that despite the increased N_2 adsorption amount than MPC-500 and MPC-950, MF-PC still exhibits mainly type I isotherm with dominantly microporous structure as compared with the hierarchically porous HPC. The comparison of MF-PC and HPC directly demonstrates the promotion effects of coal's inherent minerals on developing mesopores/macropores during CO_2 activation process.

Fig. 3b gives the N_2 isotherm derived DFT pore size distributions of tested PCs which show great consistency with the results of N_2 isotherms. More specifically, both MPCs (MPC-500 and MPC-950) and MF-PC show dominantly micropore distributions while HPC exhibits obvious pore size broadening between 2–10 nm. As summarized in Table 1, HPC possesses highest pore parameters (S_{BET} of 2308 $m^2 g^{-1}$ and V_t of 1.51 $cm^3 g^{-1}$) and obvious hierarchical pore structure. Such advantageous pore configuration of HPC originate from the synergistic effects of chemical activation and mineral-assisted CO_2 activation during which H_3PO_4 interact with coal structure to form abundant micropores at the first stage and CO_2 further etched coal structure under the catalysis of inherent minerals to form mesopores and/or macropores at the second stage.

To further demonstrate the effects of inherent minerals on the porosity development, thermogravimetric analyses (TGA) of Zhundong raw coal and demineralized Zhundong coal are conducted under the simulated CO_2 activation procedure, shown in Fig. 3c. It can be clearly seen that mineral-rich Zhundong raw coal exhibits much higher weight loss than that of demineralized Zhundong coal under temperature higher than 800 °C, suggesting the higher reactivity of Zhundong raw coal with CO_2 molecules which should greatly enhance the etching reaction between CO_2 and coal structure during activation process and thus promotes pore enlarging and the formation of well-developed hierarchical pore configuration, relative to the microporous structure derived from the weakened reaction between demineralized Zhundong coal and CO_2, as illustrated by the inset diagrams of Fig. 3c.

The chemical environments of typical samples are further investigated by the X-ray photoelectron spectroscopy (XPS) measurements. Fig. 4a displays the XPS overall spectra of HPC and MPC-500 from which all the samples exhibit peaks of C 1s, O 1s, P 2s and P 2p at the binding energies of ~287.2 eV, 536.9 eV, 131.4 eV and 189.0 eV, respectively, which indicates that except for the main carbon skeleton structure, P and O species are successfully doped in the carbon matrix. The XPS based atomic element contents of all prepared samples are summarized in Table 1 from which the oxygen and phosphorus doping levels are comparable to the values reported in the previous literature.[50,51] The high-resolution O 1s and P 2s spectra of HPC are fitted and shown in Fig. 4b and c from which the O species can be corresponded to unsaturated C–O, phenolic –OH and adsorbed water at binding energy of 531.7 eV, 533.5 eV and 534 eV, respectively,[52] while the P 2p spectrum can be divided by two peaks at binding energy of 134.5 eV and 133.5 eV, which can be assigned to C–O–PO_3 and P–O, respectively.[50,51] These doped heteroatoms are considered to be beneficial for specific capacitance owing to the followings: (1) P and O doping forms functional groups on surface of carbon, which improve the wettability and facilitates transportation of electrolyte into the interior of the carbon materials.[53,54] (2) The functional groups on the carbon surface, *e.g.* P–O, are redox active sites and can provide pseudocapacitance process to enhance specific capacitance.[55,56] (3) The heteroatom doping, *e.g.* C–O–PO_3, can change the electron density of the carbon matrix due to the difference between C and the heteroatom.[57] The P and O co-doped structure can modify the electron-donor properties which may affects the electrochemical properties synergistically.[58] In summary, the surface properties and electronic structure of carbon framework changes caused by heteroatoms improve the capacitive performances effectively.

3.3 Electrochemical performance

The electrochemical performance of the optimized HPC is examined in a three-electrode system using 6 M KOH as the electrolyte. For comparison, the microporous MPC-950 and MF-PC are also tested (MF-PC's performance was discussed in the ESI Fig. S4†). Fig. 5a shows the results of cyclic voltammetry (CV) curves of the HPC electrode at various scan rates, indicating a typical capacitive behavior. Even increasing the scan rate to 500 mV s^{-1}, HPC electrode still keeps a rather good rectangular-like CV profile, suggesting the high-rate capability (Fig. 5b). Comparatively, the MPC-950 electrode exhibits more

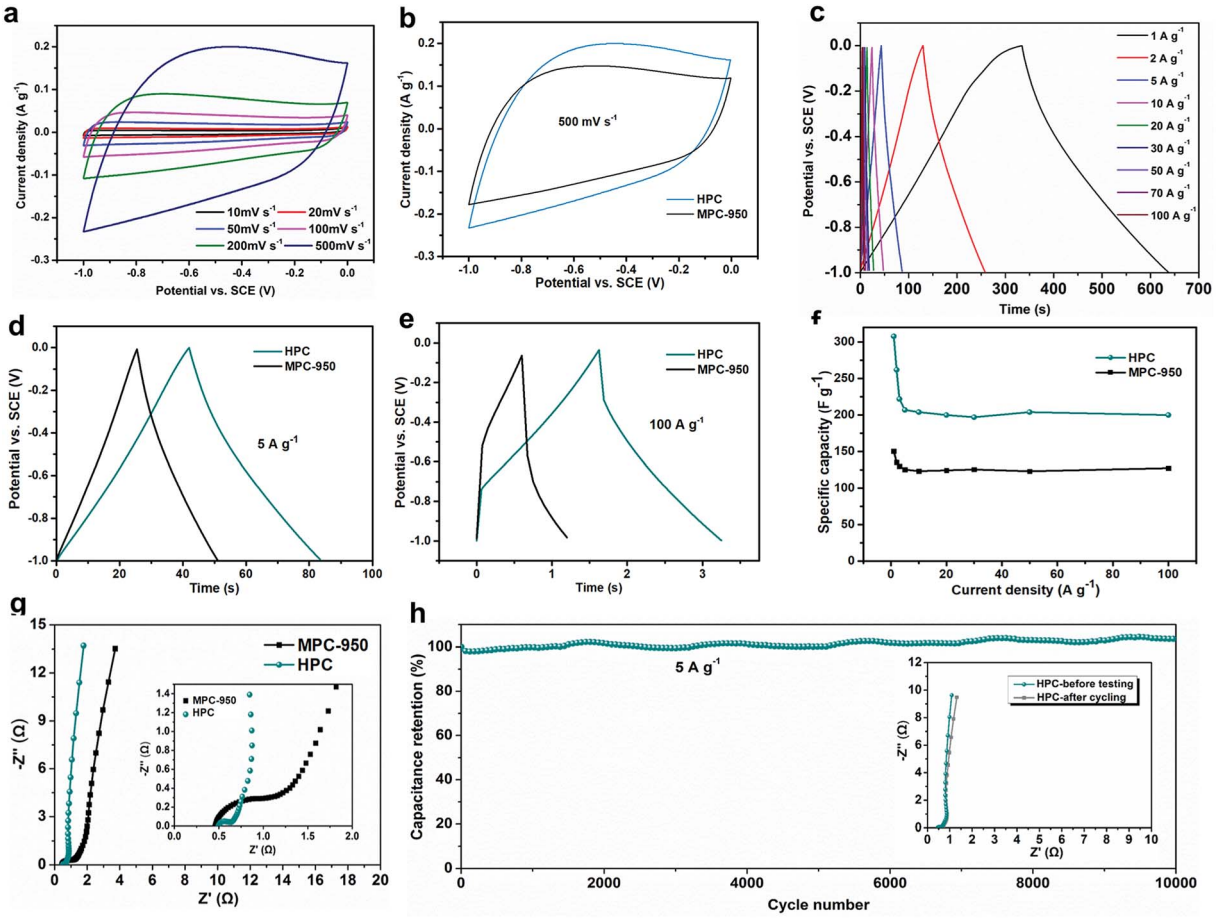

Fig. 5 Electrochemical performances of typical samples in 6 M KOH electrolyte with a three-electrode configuration. (a) CV curves at scan rates of 10–500 mV s^{-1} of HPC. (b) CV curves at a scan rate of 500 mV s^{-1} of HPC and MPC-950; (c) galvanostatic charge–discharge curves of HPC under different charge–discharge current densities; (d) galvanostatic charge–discharge curves of HPC and MPC-950 at a charge–discharge current density of 5 A g^{-1}; (e) galvanostatic charge–discharge curves of HPC and MPC-950 at a charge–discharge current density of 100 A g^{-1}; (f) gravimetric capacitances under different charge–discharge current densities of HPC and MPC-950; (g) Nyquist plot of HPC and MPC-950, inset shows the enlarged view; (h) cycling stability of HPC at a current density of 5 A g^{-1}, inset shows the Nyquist plot of HPC before and after cycling.

severe polarization than HPC electrode, especially at high scan rates (Fig. S3a† and 5b), indicating a rather inferior rate performance relative to HPC. Fig. 5c presents the galvanostatic charge–discharge curves of the HPC, with distorted linear slopes and minor voltage drops. Fig. 5d and e compare the galvanostatic charge–discharge curves of HPC and MPC-950 at 5 A g^{-1} and 100 A g^{-1}, clearly demonstrating the both higher capacitance and smaller voltage (IR) drops of HPC than those of MPC-950. Calculated form the charge–discharge curves, the gravimetric capacitance of HPC at a low current density of 1 A g^{-1} is ~308 F g^{-1}; even at an ultra-high current density of 100 A g^{-1}, the HPC still provides a gravimetric capacitance of 202 F g^{-1} with very limited IR drop of around 0.2 V. Fig. 5f further compares the rate capabilities of HPC and MPC-950 for all the tested current densities in the range of 1–100 A g^{-1}. HPC demonstrates both optimal capacitance and slower capacitance decay tendency than MPC-950. Particularly at current rates higher than 30 A g^{-1}, the HPC electrode shows near constant capacitances, indicating an ultra-fast charge–discharge performance. Such high capacitances and excellent rate performance of the HPC electrode are among the highest levels of reported carbons[59–68] tested in similar aqueous conditions (Table S3, ESI†). Considering the similar chemical environment of MPC-950 and HPC, the much improved capacitive properties of HPC should stem from the favorably hierarchical pore structure with both high surface area and pore volume which not only provide abundant electrolyte ion adsorption and storage surface, but also offer efficient electrolyte transfer and buffering channels, improving both capacitance and rate capability, relative to the microporous MPC-950 with lower specific surface area.

To further demonstrate the excellent rate capability of HPC, electrochemical impedance spectroscopy (EIS) was performed to obtain the Nyquist plots of the HPC electrode in 6 M KOH with the comparison of MPC-950 electrode, as shown in Fig. 5g. Both HPC and MPC-950 electrode exhibit straight line in the low-frequency region and a semicircle in the high-frequency region, indicating typical capacitive behaviors. Despite the similar intrinsic ohmic resistances (first intercept along the real axis) of HPC and MPC-950 electrodes, the HPC electrode shows a much smaller equivalent series resistance (ESR, by extrapolating the vertical portion to the real axis) of 0.65 Ω that of MPC-

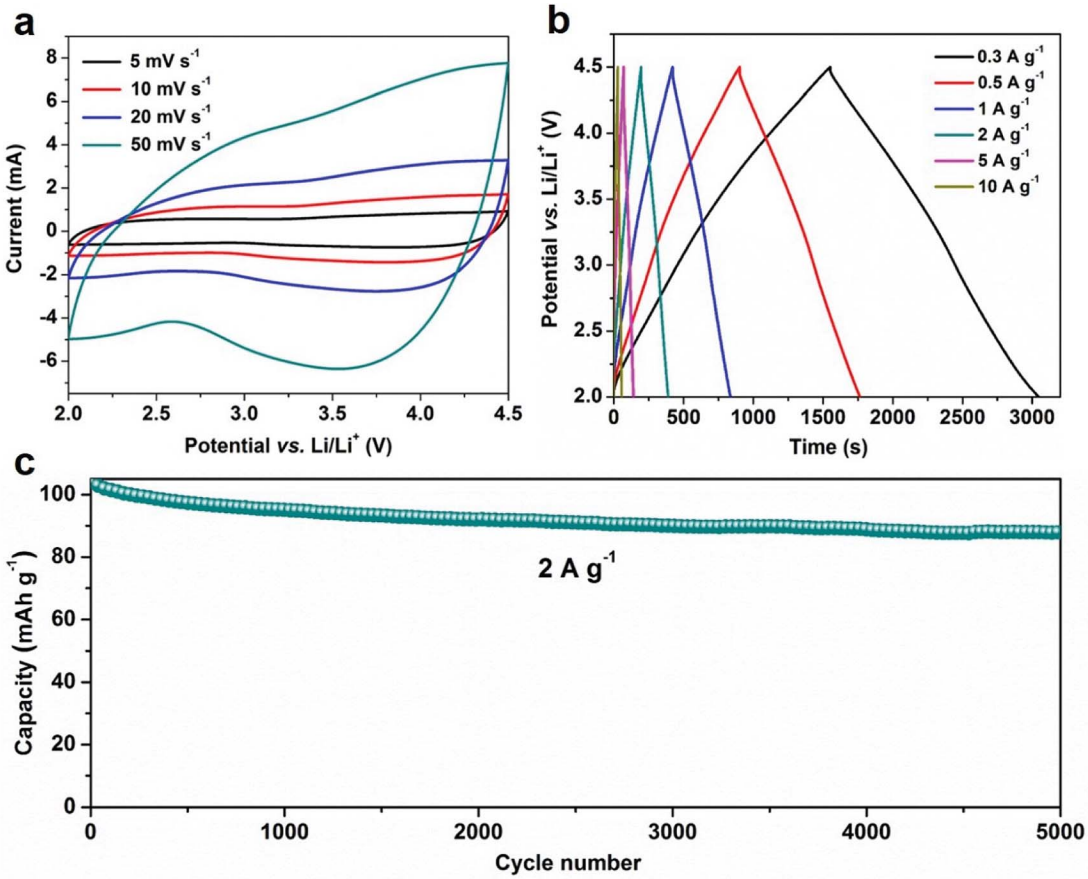

Fig. 6 (a) Electrochemical performances of HPC in 1 M $LiPF_6$ in EC/DEC electrolyte with a half-cell configuration between 2.0–4.5 V *vs.* Li/Li^+. (b) Galvanostatic charge–discharge curves of under different current densities. (c) Cycling stability at a current density of 2 A g^{-1}.

950 (1.05 Ω), demonstrating the lower contact resistance and better electrolyte accessibility of HPC electrode. Furthermore, the straight line in the low-frequency region of HPC electrode has a higher slope compared to that of the MPC-950 electrode, indicating increased ion/electron transportation. The EIS results further highlight the effect of hierarchical pore configuration on the electrolyte accessibility, increasing the rate performance. Fig. 5h and f further shows the cycling stability of HPC electrode at a current density of 5 A g^{-1} as well as the Nyquist plots of HPC electrodes before and after cycling (Fig. 5h inset). Impressively, the HPC electrode exhibits an ultra-high cycling stability with no capacity decay after 10 000 cycles. The Nyquist plots of HPC electrodes before and after cycling nearly overlap, further demonstrating its excellent cycling stability. Combining with the superior high-rate capability, as compared with literature reports (Table S3, ESI†), the HPC exhibits comprehensive improvements in supercapacitive performances as a promising candidate for aqueous supercapacitor utilization.

As well known, lithium ion capacitors (LICs), as hybrid capacitor-battery system, have been regarded as a promising choice to bridge the gap between lithium ion batteries (LIBs) and supercapacitors. LICs commonly employ a high-power supercapacitor electrode (*e.g.* activated carbon and porous carbon) as cathode, a high-energy LIBs electrode (graphite, Si/C, and metal oxides) as anode and a Li salt containing organic electrolyte.[69] For the capacitive cathode, the much lower capacity (30–35 mA h g^{-1}) of current carbon materials compared with high-capacity anodes is the key bottleneck limiting the energy density of constructed LICs.[70] As demonstrated before, the as-obtained HPC with broadened pore size distribution exhibits superior aqueously supercapacitive properties. Similarly, we consider that such well-developed pore structure of HPC is also expected to exhibit excellent performances as LIC cathodes.

Fig. 6 presents the electrochemical performances of HPC in 1 M $LiPF_6$ in EC/DEC electrolyte with a half-cell configuration between 2.0–4.5 V *vs.* Li/Li^+. Such half-cell configuration is considered as a single electrode configuration to elucidate the supercapacitive properties of the individual cathode component of LICs.[71] Fig. 6a shows the CV profiles of HPC at various scan rates, which show quasi-rectangular shapes indicating the capacitive behavior.[72,73] Increasing the scan rate will not deteriorate the CV shapes, suggesting a good rate capability. Fig. 6b shows the linear charge/discharge profiles of HPC electrode. Calculated from Fig. 6b, the capacitance/capacity of HPC electrode at various current densities can be obtained. More specifically, at a low current density of 0.3 A g^{-1}, HPC exhibit a high specific capacity of 183 F g^{-1} (127 mA h g^{-1}); even at a high current density of 10 A g^{-1}, the HPC electrode could still

delivers a gravimetric capacitance of 112 F g^{-1} (78 mA h g^{-1}), which is superior to most reported biomass-derived activated carbon cathodes, especially at high rates.[70–72,74] Moreover, the HPC electrode also exhibits a high-voltage cycling stability, as shown in Fig. 6c. As can be seen, the HPC electrode reveals 88% capacity retention after 5000 cycles at a current rate of 2 A g^{-1}. Such high capacities, excellent rate capabilities as well as high-voltage cycling stability, as far as we know, are among the highest levels of reported carbon based LIC cathodes[70,71,74–78] (refer to comparison Table S4 in ESI†), which demonstrating its promising cathode candidate for the construction of high-performance LICs.

4. Conclusion

In summary, we have demonstrated a facile preparation strategy to develop hierarchically porous carbons *via* introducing catalytic gasification mechanism into H_3PO_4 activation process using Chinese large-reserve Zhundong coal as precursor. The preparation is achieved by the synergism of mineral-assisted catalytic activation and H_3PO_4 chemical activation which are technically integrated in one-step heat-treatment procedure, leading to resulting HPC with a hierarchical pore configuration with a high surface area, a large pore volume as well as a broadened pore size distribution. Evaluated as supercapacitor electrode materials, the obtained HPC exhibits superior supercapacitive properties in both aqueous and organic systems, clearly suggesting that the tailoring of carbonaceous materials with appropriate pore configuration is very crucial to broaden the applicability in various electrolytes with different target ion sizes.

Conflicts of interest

There are no conflicts to declare.

Acknowledgements

This research was financially supported by the National Natural Science Foundation of China (Grant No. 51376054 and 51276052).

References

1 X. Wang, X. Lu, B. Liu, D. Chen, Y. Tong and G. Shen, *Adv. Mater.*, 2014, **45**(36), 4763–4782.
2 Q. Wei, F. Xiong, S. Tan, L. Huang, E. H. Lan, B. Dunn and L. Mai, *Adv. Mater.*, 2017, **29**(20), 1602300.
3 J. Wang, P. Nie, B. Ding, S. Dong, X. Hao, H. Dou and X. Zhang, *J. Mater. Chem. A*, 2016, **5**, 2411–2428.
4 Q. Wang, J. Yan and Z. Fan, *Energy Environ. Sci.*, 2016, **9**, 729–762.
5 G. Xu, P. Nie, H. Dou, B. Ding, L. Li and X. Zhang, *Mater. Today*, 2017, **20**, 191–209.
6 P. K. Nayak, L. Yang, W. Brehm and P. Adelhelm, *Angew. Chem., Int. Ed.*, 2017, **57**(1), 102–120.
7 X. Ge, Z. Li and L. Yin, *Nano Energy*, 2017, **32**, 117–124.
8 H. Kim, H. Kim, Z. Ding, M. H. Lee, K. Lim, G. Yoon and K. Kang, *Adv. Energy Mater.*, 2016, **6**, 1600943.
9 M. Salanne, B. Rotenberg, K. Naoi, K. Kaneko, P. L. Taberna, C. P. Grey, B. Dunn and P. Simon, *Nat. Energy*, 2016, **1**, 16070.
10 F. Sun, L. Wang, Y. Peng, J. Gao, X. Pi, Z. Qu, G. Zhao and Y. Qin, *Appl. Surf. Sci.*, 2018, **436**, 486–494.
11 F. Sun, J. Gao, Y. Zhu, X. Pi, L. Wang, X. Liu and Y. Qin, *Sci. Rep.*, 2017, **7**, 40990.
12 T. Y. Ma, L. Liu and Z. Y. Yuan, *Chem. Soc. Rev.*, 2013, **42**, 3977–4003.
13 S. Dutta, A. Bhaumik and K. C. W. Wu, *Energy Environ. Sci.*, 2014, **7**, 3574–3592.
14 Y. Li, K. Zhang, S. A. A. Shah, Y. Huang, Y. TIan, J. Cheng and J. Zhang, *RSC Adv.*, 2017, **7**(69), 43356–43365.
15 M. Serwar, U. A. Rana, H. M. Siddiqi, S. U. D. Khan, F. A. A. Ali, A. Al-Fatech, A. Adomkevicius, J. A. Coca-Clemente, L. Cabo-Fernandez, F. Braga and L. J. Hardwick, *RSC Adv.*, 2017, **7**, 54626–54637.
16 X. Zhang, Y. Jiao, L. Sun, L. Wang, A. Wu, H. Yan, M. Meng, C. TIan, B. Jiang and H. Fu, *Nanoscale*, 2016, **8**, 2418–2427.
17 L. Sun, L. Wang, C. Tian, T. Tan, Y. Xie, K. Shi, M. Li and H. Fu, *RSC Adv.*, 2012, **2**(10), 4498–4506.
18 J. Wang, H. Liu, H. Sun, W. Wang, X. Liu and B. Wei, *Carbon*, 2018, **127**, 85–92.
19 B. Wang, Y. Wang, Y. Peng, X. Wang, N. Wang, J. Wang and J. Zhao, *J. Chem. Eng.*, 2018, **348**, 850–859.
20 Y. Wen, B. Wang, C. Huang, L. Wang and D. Hulicova-Jurcakova, *Chemistry*, 2015, **21**(1), 80–85.
21 Z. Ling, Z. Wang, M. Zhang, C. Yu, G. Wang, Y. Dong, S. Liu, Y. Wang and J. Qiu, *Adv. Funct. Mater.*, 2016, **26**, 111–119.
22 A. Elmouwahidi, J. Castelo-Quibén, J. F. Vivo-Vilches, A. F. Pérez-Cadenas, F. J. Maldonado-Hódara and F. Carrasco-Marín, *Chem. Eng. J.*, 2018, **334**, 1835–1841.
23 Q. L. Zhu, P. Pachfule, P. Strubel, Z. Li, R. Zou, Z. Liu, S. Kaskel and Q. Xu, *Energy Storage Materials*, 2018, **13**, 72–79.
24 G. Xu, J. Han, B. Ding, P. Nie, J. Pan, H. Dou, H. Li and X. Zhang, *Green Chem.*, 2015, **17**, 1668–1674.
25 S. Y. Lu, M. Jin, Y. Zhang, Y. B. Niu, J. C. Chang and C. M. Li, *Adv. Energy Mater.*, 2017, 1702545.
26 S. Gao, Y. Tang, L. Wang, L. Liu, Z. Sun, S. Wang, H. Zhao, L. B. Kong and D. Jia, *ACS Sustainable Chem. Eng.*, 2018, **6**(3), 3255–3263.
27 J. Wang and S. Kaskel, *J. Mater. Chem.*, 2012, **22**, 23710.
28 Y. Lv, F. Zhang, Y. Dou, Y. Zhai, J. Wang, H. Liu, Y. Xia, B. Tu and D. Zhao, *J. Mater. Chem.*, 2012, **22**, 93–99.
29 F. Sun, J. Gao, X. Liu, X. Pi, Y. Yang and S. Wu, *Appl. Surf. Sci.*, 2016, **387**, 857–863.
30 L. Yue, Q. Xia, L. Wang, L. Wang, H. DaCosta, J. Yang and X. Hu, *J. Colloid Interface Sci.*, 2018, **511**, 259–267.
31 H. Sayğılı and F. Güzel, *J. Cleaner Prod.*, 2016, **113**, 995–1004.
32 H. Chen, H. Wei, N. Fu, W. Qian, Y. Liu, H. Lin and S. Han, *J. Mater. Sci.*, 2017, **53**, 2669–2684.
33 Y. Kan, Q. Yue, S. Liu and B. Gao, *Chem. Eng. J.*, 2018, **331**, 93–101.

34 F. J. Garcíamateos, R. Berenguer, M. J. Valeroromero, J. Rodríguezmirasol and T. Cordero, *J. Mater. Chem. A*, 2018, **6**, 1219–1233.
35 K. Zhang, Y. Li, Z. Wang, Q. Li, R. Whiddon, Y. He and K. Cen, *Fuel*, 2016, **185**, 701–708.
36 M. A. Yahya, Z. Al-Qodah and C. W. Z. Ngah, *Renewable Sustainable Energy Rev.*, 2015, **46**, 218–235.
37 V. Fierro, V. Torné-Fernández and A. Celzard, *Microporous Mesoporous Mater.*, 2006, **92**, 243–250.
38 M. Molina-sabio, F. Rodríguez-reinoso, F. Caturla and M. J. Sellés, *Carbon*, 1995, **33**(8), 1105–1113.
39 V. Fierro, V. Torné-Fernández, D. Montané and A. Celzard, *Thermochim. Acta*, 2005, **433**(1), 142–148.
40 M. S. Solum, R. J. Pugmire, M. Jagtoyen and F. Derbyshire, *Carbon*, 1995, **33**(9), 1247–1254.
41 P. Cheng, S. Gao, P. Zang, X. Yang, Y. Bai, H. Xu, Z. Liu and Z. Lei, *Carbon*, 2015, **93**, 315–324.
42 T. H. Liou, *Chem. Eng. J.*, 2010, **158**, 129–142.
43 P. Lahijani, Z. A. Zainal, M. Mohammadi and A. R. Mohamed, *Renewable Sustainable Energy Rev.*, 2015, **46**(39), 615–632.
44 K. Xia, Q. Gao, J. Jiang and J. Hu, *Carbon*, 2008, **46**(13), 1718–1726.
45 P. Lahijani, Z. A. Zainal, A. R. Mohamed and M. Mohammadi, *Bioresour. Technol.*, 2013, **144**(3), 288–295.
46 S. Yuan, X. Chen, J. Li and F. Wang, *Energy Fuels*, 2011, **25**(5), 2314–2321.
47 L. S. Lobo and S. A. C. Carabineiro, *Fuel*, 2016, **183**, 457–469.
48 W. Ergun, J. B. Yasinsky and J. R. Townsend, *Carbon*, 1967, **5**(4), 403–408.
49 L. Wang, F. Sun, J. Gao, X. Pi, Z. Qu and G. Zhao, *Energy Fuels*, 2018, **32**(2), 1255–1264.
50 D. S. Yang, D. Bhattacharjya, S. Inamdar, J. Park and J. S. Yu, *J. Am. Chem. Soc.*, 2012, **134**, 16127–16130.
51 X. Xu, W. Yang, B. Chen, C. Zhou, X. Ma, L. Hou, Y. Tang, F. Yang, G. Ning, L. Zhang and Y. Li, *Appl. Surf. Sci.*, 2017, **405**, 308–315.
52 R. Rasuli, Z. Mokarian, R. Karimi, H. Shabanzadeh and Y. Abedini, *Thin Solid Films*, 2015, **589**, 364–368.
53 Z. Xu, Y. Liu, H. Chen, M. Yang and H. Li, *J. Mater. Sci.*, 2017, **52**, 7781–7793.
54 X. Yu, Y. Kang and H. S. Park, *Carbon*, 2016, **101**, 49–56.
55 J. P. Paraknowitsch and A. Thomas, *Energy Environ. Sci.*, 2013, **6**(10), 2839–2855.
56 X. Yu, H. J. Kim, J. Y. Hong, Y. M. Jung, K. D. Kwon, J. Kong and H. S. Park, *Nano Energy*, 2015, **15**, 576–586.
57 J. Y. Hong, J. J. Wie, Y. Xu and H. S. Park, *Phys. Chem. Chem. Phys.*, 2015, **17**(46), 30946–30962.
58 Y. Wang, Y. Wu, K. Lina, A. Song, X. Qin and G. Shao, *Carbon*, 2018, **127**, 557–567.
59 L. Sun, C. Tian, Y. Fu, Y. Yang, J. Yin, L. Wang and H. Fu, *Chem.–Eur. J.*, 2014, **20**, 564.
60 D. Zhang, L. Zheng, Y. Ma, L. Lei, Q. Li, Y. Li, H. Luo, H. Feng and Y. Hao, *ACS Appl. Mater. Interfaces*, 2014, **6**, 2657–2665.
61 L. F. Chen, X. D. Zhang, H. W. Liang, M. Kong, Q. F. Guan, P. Chen, Z. Y. Wu and S. H. Yu, *ACS Nano*, 2012, **6**, 7092.
62 N. P. Wickramaratne, J. Xu, M. Wang, L. Zhu, L. Dai and M. Jaroniec, *Chem. Mater.*, 2014, **26**, 2820–2828.
63 J. Wei, D. Zhou, Z. Sun, Y. Deng, Y. Xia and D. Zhao, *Adv. Funct. Mater.*, 2013, **23**, 2322–2328.
64 W. Qian, F. Sun, Y. Xu, L. Qiu, C. Liu, S. Wang and F. Yan, *Energy Environ. Sci.*, 2013, **7**, 379–386.
65 W. Chen, R. B. Rakhi, M. N. Hedhili and H. N. Alshareef, *J. Mater. Chem. A*, 2014, **2**, 5236–5243.
66 Z. Li, Z. Xu, X. Tan, H. Wang, C. M. B. Holt, T. Stephenson, B. C. Olsen and D. Mitlin, *Energy Environ. Sci.*, 2013, **6**, 871–878.
67 X. Fan, C. Yu, J. Yang, Z. Ling, C. Hu, M. Zhang and J. Qiu, *Adv. Energy Mater.*, 2015, **5**, 1401761.
68 H. Sun, W. He, C. Zong and L. Lu, *ACS Appl. Mater. Interfaces*, 2013, **5**, 2261–2268.
69 B. Li, F. Dai, Q. Xiao, L. Yang, J. Shen, C. Zhang and M. Cai, *Adv. Energy Mater.*, 2016, **6**, 1600802.
70 H. Wang, Y. Zhang, H. Ang, Y. Zhang, H. T. Tan, Y. Zhang, Y. Guo, J. B. Franklin, X. L. Wu, M. Srinivasan, H. J. Fan and Q. Yan, *Adv. Funct. Mater.*, 2016, **26**, 3082–3093.
71 A. Jain, V. Aravindan, S. Jayaraman, P. S. Kumar, R. Balasubramanian, S. Ramakrishna, S. Madhavi and M. P. Srinivasan, *Sci. Rep.*, 2013, **3**, 3002.
72 R. Yi, S. Chen, J. Song, M. L. Gordin, A. Manivannan and D. Wang, *Adv. Funct. Mater.*, 2014, **24**, 7433–7439.
73 B. Li, F. Dai, Q. Xiao, L. Yang, J. Shen, C. Zhang and M. Cai, *Energy Environ. Sci.*, 2015, **9**, 102–106.
74 Q. Xia, H. Yang, M. Wang, M. Yang, Q. Guo, L. Wan, H. Xia and Y. Yu, *Adv. Energy Mater.*, 2017, 1701336.
75 M. Schroeder, M. Winter, S. Passerini and A. Balducci, *J. Power Sources*, 2013, **238**, 388–394.
76 G. Wang, C. Lua, X. Zhang, B. Wan, H. Liu, M. Xia, H. Gou, G. Xin, J. Lian and Y. Zhang, *Nano Energy*, 2017, **36**, 46–57.
77 L. Ye, Q. Liang, Y. Lei, X. Yu, C. Han, W. Shen, Z. Huang, F. Kang and Q. Yang, *J. Power Sources*, 2015, **282**, 174–178.
78 A. Yoshino, T. Tsubata, M. Shimoyamada, H. Satake, Y. Okano, S. Mori and S. Yata, *J. Electrochem. Soc.*, 2004, **151**(12), A2180–A2182.